



Flexible, low-loss, large-area, wide-angle, wavelength-selective plasmonic multilayer metasurface

Ping-Chun Li and Edward T. Yu

Citation: *J. Appl. Phys.* **114**, 133104 (2013); doi: 10.1063/1.4824371

View online: <http://dx.doi.org/10.1063/1.4824371>

View Table of Contents: <http://jap.aip.org/resource/1/JAPIAU/v114/i13>

Published by the [AIP Publishing LLC](#).

Additional information on *J. Appl. Phys.*

Journal Homepage: <http://jap.aip.org/>

Journal Information: http://jap.aip.org/about/about_the_journal

Top downloads: http://jap.aip.org/features/most_downloaded

Information for Authors: <http://jap.aip.org/authors>

ADVERTISEMENT

Read author interviews in **Bookends**

Flexible, low-loss, large-area, wide-angle, wavelength-selective plasmonic multilayer metasurface

Ping-Chun Li and Edward T. Yu^{a)}

Microelectronics Research Center, University of Texas at Austin, 10100 Burnet Rd., Austin, Texas 78758, USA

(Received 29 July 2013; accepted 20 September 2013; published online 2 October 2013)

Flexible, low-loss, large-area multilayer plasmonic optical metasurfaces are demonstrated and analyzed that provide wavelength-selective reflectance $>95\%$ and transmittance $<1\%$ with low absorption and robustness to variation in angle of incidence and polarization. These characteristics are shown to be insensitive to vertical misalignment between layers, and defects within individual layers. Analysis based on analytical modeling and numerical simulations provides physical insights into reflectance, loss, and bandwidth of these multilayer metasurface structures. Fabry-Perot resonances associated with phase shifts from each individual metasurface are also examined, and evidence of $m=0$ resonance due to the nonzero, wavelength dependent phase shift from the metasurface cavity is demonstrated and explained. Finally, fabrication on flexible substrates via rapid, large-area nanosphere lithography, and the robustness of optical properties of interlayer misalignment together enable the demonstration of wavelength-selective focusing at optical frequencies. © 2013 AIP Publishing LLC. [<http://dx.doi.org/10.1063/1.4824371>]

I. INTRODUCTION

Manipulation of light via plasmonic behavior in subwavelength metallic nanostructures is currently a subject of intense research interest and is enabling the development of nanostructured metamaterials and metasurfaces that provide a variety of new optical and electromagnetic functionalities, or that enable existing functionalities to be realized in new and often extremely compact form factors.^{1–4} Most such concepts involve structures fabricated in a rigid, single-layer, planar geometry.^{5–11} However, three-dimensional plasmonic nanostructures have been shown to enable additional possibilities for engineering optical chirality,¹² negative refractive indices,¹³ and molecular sensing behavior.¹⁴ Furthermore, interest in highly nonplanar geometries and fabrication on flexible or stretchable substrates^{15–18} has been fueled by applications, such as transformation optics,¹⁹ cloaking,^{20,21} and imaging.²² The ability to fabricate plasmonic nanostructures with multiple plasmonic layers, over large areas, and on flexible substrates could enable the realization of additional new optical functionalities, and the application of plasmonic nanostructures in a broad range of new settings in which structural flexibility, conformation to curved or irregular surfaces, large areas, or low cost is required.

In this paper, we report the design, fabrication, experimental demonstration, and analysis of multilayer optical metasurfaces over large areas ($\sim 4\text{--}8\text{ cm}^2$) on flexible polymer substrates. These structures are shown to provide wavelength-selective reflectance and transmittance with low absorption loss that is robust to variations in polarization and in angle of incidence. Furthermore, fabrication on flexible polymer substrates enables capabilities, such as wavelength-selective focusing to be achieved, and the use of rapid, large-area nanoscale patterning techniques, and the

robustness of optical properties to misalignment between vertically stacked layers make these structures highly promising for applications in which low cost and large area are desirable or essential.

II. EXPERIMENT

Figure 1(a) shows a schematic diagram of a two-layer metasurface structure, the measurement geometry employed for transverse electric (TE), and transverse magnetic (TM) polarizations, and a scanning electron microscope (SEM) image of a completed structure. As indicated in the figure, individual metallic elements of diameter D and thickness d that constitute each metasurface layer are arranged in a hexagonal array with center-to-center spacing P between adjacent elements. A SiO_2 layer of thickness h is present below each hexagonal array layer, and an SU-8 layer of thickness H is present between successive metasurface layers. All structures were fabricated on polyethylene terephthalate (PET) films (Dupont Melinex 454). Key steps in the fabrication process for each metasurface layer are shown in Figures 1(b)–1(d). First, 10 nm SiO_2 /100 nm liftoff resist (LOR)/10 nm SiO_2 is deposited. The two layers of SiO_2 were deposited in separate e-beam evaporation processes. A self-assembled monolayer of 200 nm-diameter polystyrene (PS) spheres is then deposited on the SiO_2 surface using the Langmuir-Blodgett method,^{23,24} as shown in Figure 1(b). Reactive ion etching (RIE) is then used to etch the PS spheres, thereby reducing their diameter to $\sim 160\text{ nm}$, after which 20 nm Cr is deposited by e-beam evaporation. The nanospheres are then removed by a lift-off process in toluene, resulting in formation of a Cr hard mask consisting of a hexagonal array of holes, within which the underlying LOR/ SiO_2 layers are removed by RIE, resulting in the structure shown in Figure 1(c). Finally, 5 nm Ge/40 nm Ag metalization is deposited by e-beam evaporation, followed by

^{a)}ety@ece.utexas.edu

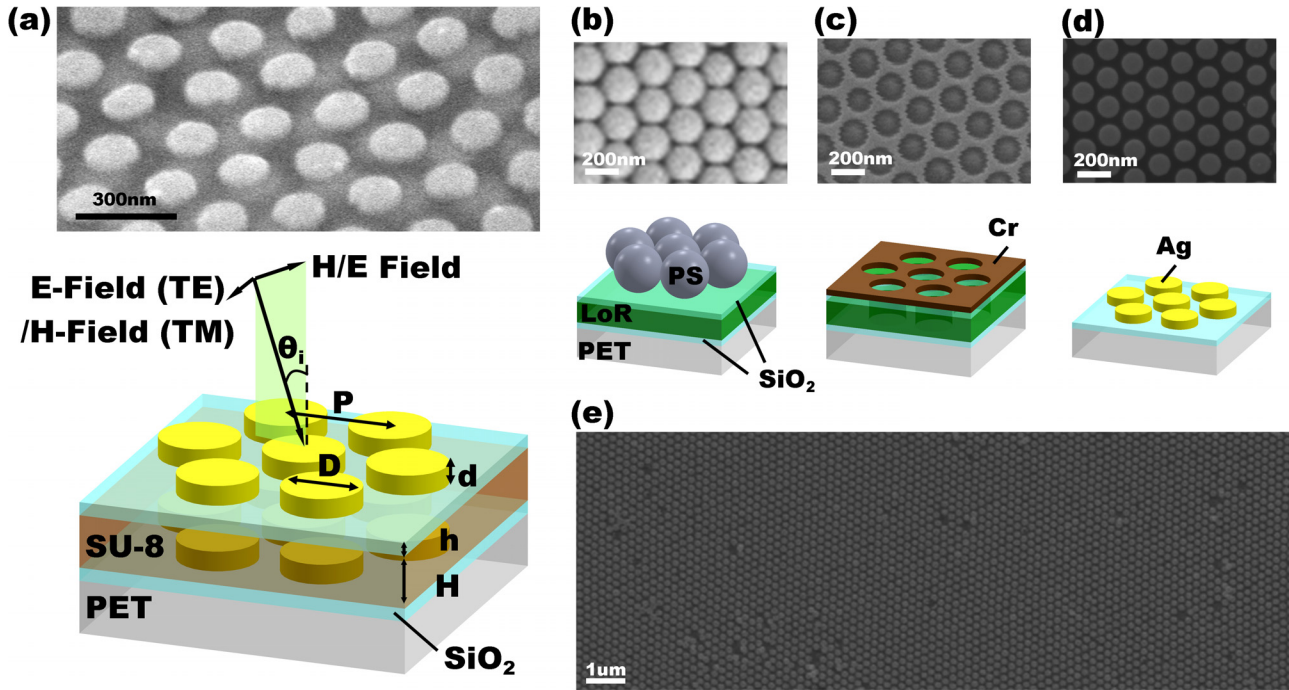


FIG. 1. (a) Schematic diagram of the multilayer metasurface structure on a PET substrate under TE and TM polarized illumination. P , D , and d indicate the periodicity of the array, size, and thickness of the individual metallic nanostructure. The thickness of SU-8 and SiO₂ is denoted as H and h , respectively. The inset shows a scanning electron micrograph of a fabricated sample with $P = 200$ nm, $D = 160$ nm, $d = 40$ nm, $h = 10$ nm, and $H = 185$ nm. (b)–(d) Schematic diagram of the fabrication process flow and scanning electron micrograph at each step: (b) A PET substrate is covered with 10 nm SiO₂/100 nm LoR/10 nm SiO₂, followed by NSL using $D = 200$ PS nanospheres. (c) After deposition of 20 nm of Cr and lift-off process of PS, the substrate is etched by RIE to create a hexagonal hole array structure. (d) The hexagonal hole array patterned PET substrate is deposited with 5 nm Ge/40 nm Ag, and the LoR is removed by lift-off process. (e) Large-area ($6 \times 16 \mu\text{m}^2$) scanning electron micrograph image to show representative defects which can result from NSL.

lift-off to create a hexagonal array of Ag disks as shown in Figure 1(d). Between successive metasurface layers, an SU-8 dielectric layer is deposited by spin-coating, which also serves to planarize the surface for fabrication of the subsequent metasurface layer. Figure 1(e) shows a large-area SEM image of a completed structure, in which a number of individual and clustered point defects in the hexagonal array are present. At larger length scales, well-ordered hexagonal grains with a typical lateral dimension of $\sim 100 \mu\text{m}$ become evident.

Optical transmittance measurements were performed using collimated light from a halogen lamp spectrally resolved by a monochromator. The monochromatic light was linearly polarized by a Glan-Thompson polarizer before reaching the samples, which were mounted on a rotating clamp microstage, allowing measurements to be performed at different incident angles (θ_i) and curvature. Numerical simulations of the optical behavior of these structures were performed using rigorous coupled wave analysis (RCWA).²⁵ The dielectric properties of Ag and SiO₂ were modeled using the Lorentz-Drude model with material parameters from the published literature that are known to correspond well to experimental measurements.^{26,27} The refractive indices of SU-8 and PET are both assumed to be 1.60 and non-dispersive.

III. RESULTS AND DISCUSSION

Previous work has shown^{28,29} that single- and double-layer metasurface structures consisting of square arrays of nanoscale metallic elements on glass substrate can provide

wavelength-selective transmittance and reflectance at optical wavelengths that are insensitive to polarization and angle of incidence, with a double-layer metasurface able to provide low ($< 1\%$) transmittance and high ($> 75\%$) reflectance over a bandwidth of ~ 100 nm. As shown here, a large increase in bandwidth can be achieved with hexagonal rather than square arrays. Figures 2(a) and 2(b) show experimentally measured transmittance T and reflectance R , along with the implied absorption $A = 1 - R - T$, for a single-layer metasurface with $D = 160$ nm, $P = 200$ nm, $d = 40$ nm, and $h = 10$ nm for normal incidence. A minimum in transmittance (maximum in reflectance) is observed at ~ 605 nm with a full-width half-maximum (FWHM) bandwidth of ~ 300 nm. Because this behavior is associated with the dipolar plasmonic resonance in an individual Ag disc as confirmed by numerical simulations shown in Figures 2(c) and 2(d), it is very weakly dependent on polarization of the incident light,^{30–32} and also insensitive to defects in the hexagonal array associated with the nanosphere lithography patterning process. These features are similar to those observed in a single-layer square plasmonic metasurface array with similar dimensions,²⁸ for which a transmittance minimum was observed centered at ~ 650 nm with a bandwidth of ~ 200 nm. As described below, we attribute the increase in bandwidth for the hexagonal array compared with the square array to stronger coupling among individual Ag plasmonic elements associated with a higher geometrical fill factor in the former. Figures 2(e) and 2(f) show the measured transmittance, reflectance, and absorption as a function of θ_i from 15° to 60° under TE and TM polarized

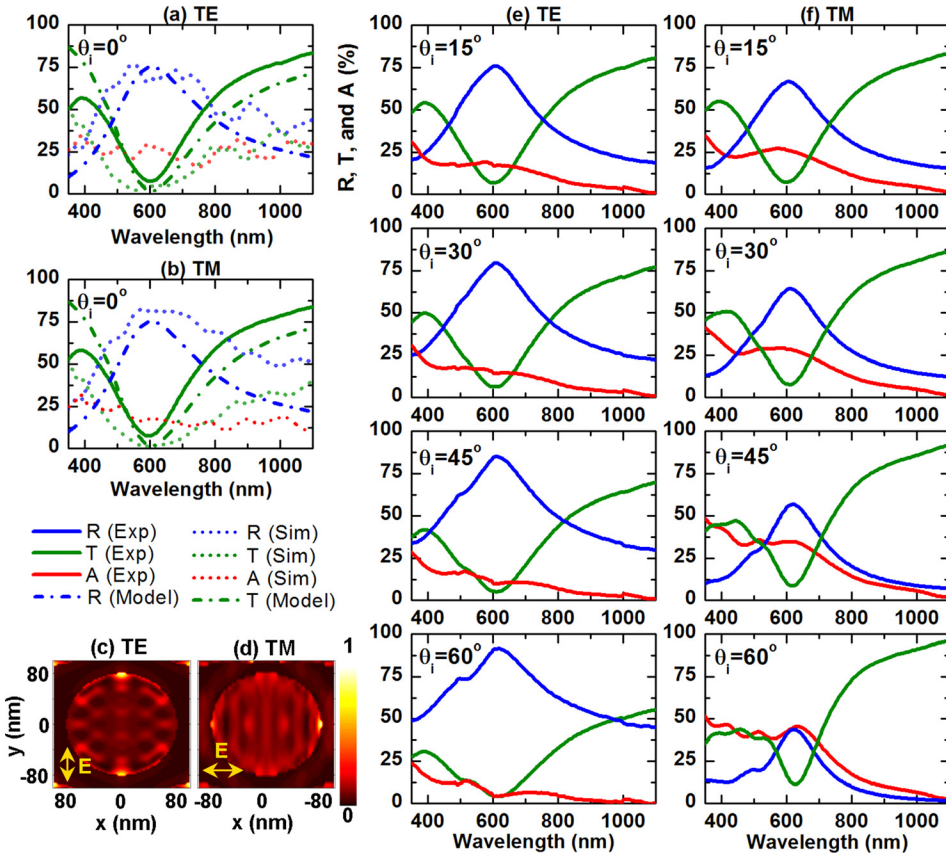


FIG. 2. (a) and (b) Measured, simulated, and modelled reflectance (R), transmittance (T), and absorption (A) spectra for a single layer metasurface with $P = 200$ nm, $D = 160$ nm, $d = 40$ nm, and $h = 10$ nm for $\theta_i = 0^\circ$ under TE and TM polarized illumination, respectively. (c) and (d) Normalized electric field distribution of the metasurface structure at resonant wavelength ($\lambda = 605$ nm) for $\theta_i = 0^\circ$ under TE and TM polarized illumination, respectively. (e) and (f) Measured reflectance (R), transmittance (T), and absorption (A) spectra for a single layer metasurface with $P = 200$ nm, $D = 160$ nm, $d = 40$ nm, and $h = 10$ nm for $\theta_i = 15^\circ, 30^\circ, 45^\circ$, and 60° under TE and TM polarized illumination, respectively.

illumination. The resonance at 605 nm shows very weak dependence on angle of incidence consistent with our previous work.²⁹

Analytical modeling of the optical response of a single-layer metasurface as an optically thin, polarization-independent homogeneous planar resonator can provide physical insight into the behavior of such structures, and a basis for rapid design and approximate modeling of multilayer metasurfaces.³³ Briefly, an effective susceptibility $\chi(\lambda)$ of the metasurface layer is defined, and assumed to be given by a Lorentzian lineshape function^{34,35}

$$\chi(\lambda) = -\frac{\Gamma(\lambda_r/\lambda)}{hc(1/\lambda - 1/\lambda_r) + i\gamma}, \quad (1)$$

where h is Planck's constant, c is the speed of light in vacuum, Γ is a radiative linewidth, γ is a nonradiative linewidth, and λ_r is the resonant wavelength. From Eq. (1), we see that Γ is associated with the amplitude and broadening of the susceptibility at the resonant wavelength, consistent with the correlation between increased geometric fill factor and resonance bandwidth described above. The corresponding amplitudes of electromagnetic plane waves reflected by and transmitted across a single metasurface layer at normal incidence, $r(\lambda)$ and $t(\lambda)$, respectively, can be computed using a standard transfer matrix approach and are then given by

$$r(\lambda) = \frac{i\Gamma}{hc(1/\lambda - 1/\lambda_r) + i(\gamma + \Gamma)}, \quad (2)$$

$$t(\lambda) = \frac{hc(1/\lambda - 1/\lambda_r) + i\gamma}{hc(1/\lambda - 1/\lambda_r) + i(\gamma + \Gamma)}. \quad (3)$$

The reflectance R and transmittance T are then given by $R = |r|^2$ and $T = |t|^2$, respectively. Fitting these functions to the experimentally measured transmittance at normal incidence, shown in Figure 2, yields $\lambda_r = 605$ nm, $\Gamma = 0.513$ eV, and $\gamma = 0.0794$ eV, and the resulting modeled transmittance is seen to be in good agreement with the experimentally measured results.

This analytical model can be extended in a straightforward manner³³ to design and analysis of multilayer metasurface structures. Figure 3 shows measured transmittance, analytically modeled transmittance and reflectance, and numerically simulated transmittance, reflectance, and absorption, at normal incidence with TE or TM polarization, for a multilayer structure containing two Ag metasurface layers, each with $P = 200$ nm, $D = 160$ nm, $d = 40$ nm, and $h = 10$ nm, separated by an SU-8 dielectric layer with $H = 185$ nm. Also shown are measured transmittance and reflectance, along with implied absorption, as a function of angle of incidence θ_i from 0° (normal incidence) to 60° . A very high, broad reflectance band is observed with peak reflectance near 650 nm of $\sim 90\%$ or higher for angles of incidence ranging from 0° to 45° and for both TE and TM polarization. Bandwidth (FWHM) of ~ 400 nm centered at ~ 650 nm is maintained for the measured high-reflectance band for both polarizations and over angles of incidence ranging from 0° to 45° .

The high, broad reflectance feature observed experimentally can be explained as a consequence of Bragg reflection by the multilayer metasurface structure using the analytical model described above. In general, the Bragg reflection criterion will be satisfied, and high reflectance will be observed,

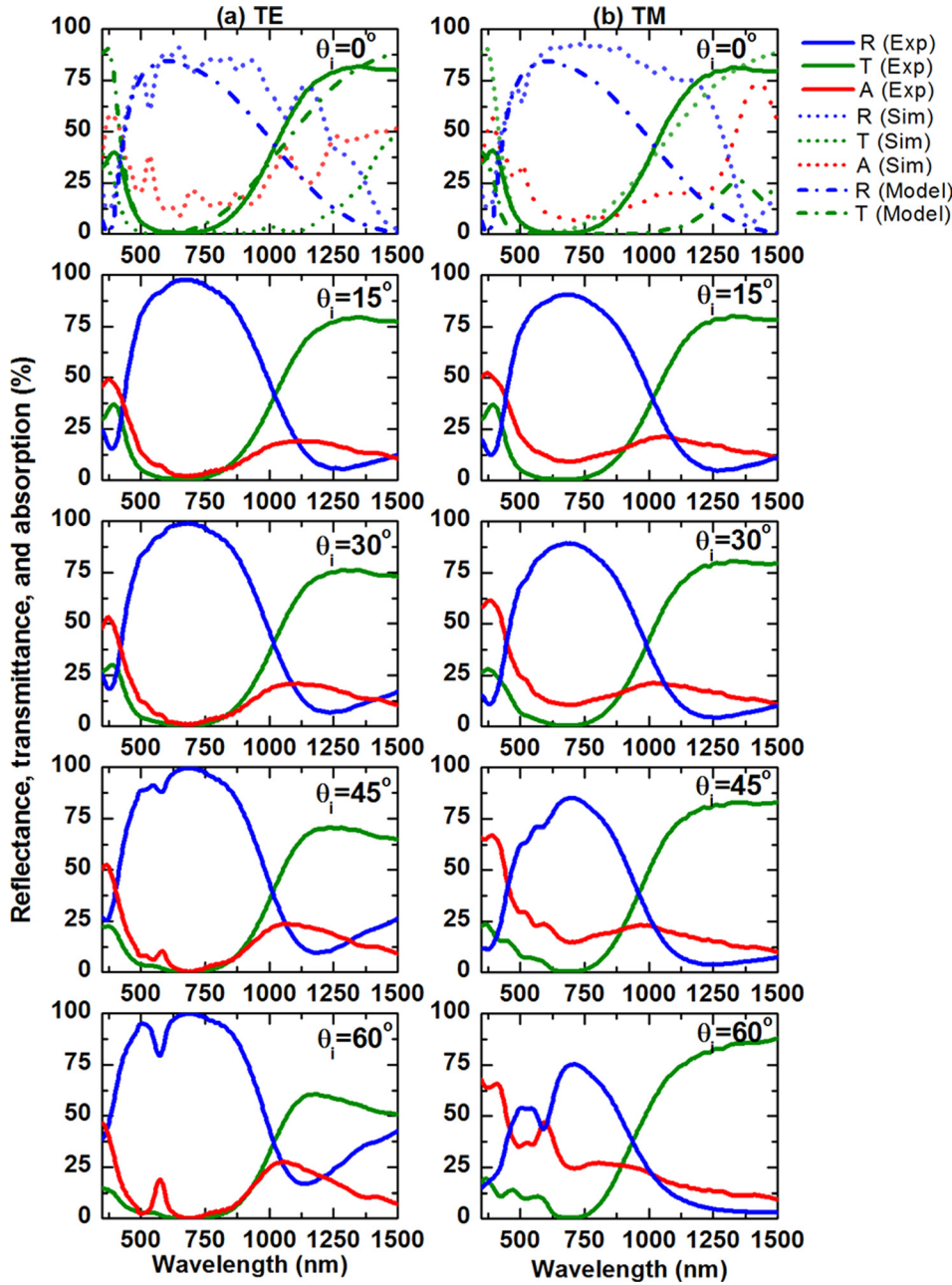


FIG. 3. (a) and (b) Measured, simulated, and modelled reflectance, transmittance, and absorption spectra for a double layer metasurface with $P = 200$ nm, $D = 160$ nm, $d = 40$ nm, $h = 10$ nm, and $H = 185$ nm for $\theta_i = 0^\circ, 15^\circ, 30^\circ, 45^\circ,$ and 60° under TE and TM polarized illumination.

when the electromagnetic waves reflected by each individual metasurface layer are in phase with each other. According to Eq. (1), the wave component reflected from each metasurface layer will in general include a phase shift $\phi(\lambda)$ given by

$$\phi(\lambda) = \tan^{-1} \left(\frac{\text{Im}(r)}{\text{Re}(r)} \right) = \tan^{-1} \left(\frac{hc(1/\lambda - 1/\lambda_r)}{\gamma + \Gamma} \right). \quad (4)$$

At the resonance wavelength $\lambda_r = 605$ nm, however, this phase shift vanishes, so that the Bragg criterion will be satisfied for $H + h = \lambda/2n_d \approx 190$ nm, where $n_d = 1.6$ is the refractive index of the dielectric separating the metasurface layers. For the two-layer metasurface structure of Figure 2, $H + h = 185$ nm + 10 nm = 195 nm, allowing constructive interference due to Bragg reflection at and near the resonance wavelength to increase the peak reflectance, and broaden the reflectance peak, compared with that for a single-layer

structure.³³ The performance of multilayer metasurfaces is superior to that of conventional thin film Bragg reflectors^{36,37} which have very limited angle of incidence acceptance and usually require many dielectric layers to achieve high reflectance. These characteristics of traditional Bragg reflectors properties will also restrict the use of thin film Bragg reflectors on curved surfaces.

We also observe that the width of the high-reflectance peak is close to its photonic bandgap, reached in the limit of an infinite periodic metasurface/dielectric stack, given by³³

$$\lambda_{min} = \frac{1}{\frac{1}{\lambda_r} + \sqrt{\frac{2\Gamma}{\pi hc \lambda_r}}} < \lambda < \frac{1}{\frac{1}{\lambda_r} - \sqrt{\frac{2\Gamma}{\pi hc \lambda_r}}} = \lambda_{max}, \quad (5)$$

where $\lambda_{max} - \lambda_{min}$ is the FWHM bandwidth of the reflectance peak. For the single-layer metasurface parameters $\lambda_r = 605$ nm and $\Gamma = 0.513$ eV, derived from Eq. (3) and the data in Figure 2,

we obtain $\lambda_{min} = 432$ nm, $\lambda_{max} = 1006$ nm, corresponding to a FWHM bandwidth $\lambda_{max} - \lambda_{min} = 564$ nm. The measured FWHM of the reflectance peaks for angles of incidence up to 30° is ~ 550 nm, close to the theoretical limit estimated from our analytical model and suggesting that bandwidth close to the photonic bandgap for a periodic multilayer metasurface structure can be achieved with as few as two metasurface layers. A detailed analysis employing the multilayer metasurface analytical model³³ is also consistent with this observation.

Phase shifts associated with reflectance by each metasurface layer also influence the nature of Fabry-Perot resonances and associated increases in absorption in multilayer metasurface structures. Figures 4(a) and 4(b) show numerically simulated reflectance, for TE polarized light, of a multilayer structure with two metasurface layers separated by an SU-8 dielectric layer, as a function of wavelength and dielectric thickness H , for angles of incidence of 15° and 60° . Each metasurface layer consists of a hexagonal array of Ag discs with $P = 200$ nm, $D = 160$ nm, and $d = 40$ nm, atop a SiO_2 layer of thickness $h = 10$ nm. For a given H , the numerically simulated reflectance exhibits local minima as a function of wavelength that can be attributed to Fabry-Perot resonances created by reflection from each metasurface layer. Accounting for the wavelength-dependent phase shift introduced upon each reflection from a metasurface layer, the wavelengths for which Fabry-Perot resonances occur are given by^{29,38}

$$\lambda = \frac{2\sqrt{n_d^2 - \sin^2\theta_i}}{m - \phi(\lambda)/\pi} (H + h), \quad (6)$$

where m is a non-negative integer corresponding to different Fabry-Perot modes, n_d and H are the refractive index and thickness, respectively, of the SU-8 dielectric spacer layer,

and $\phi(\lambda)$ is given by Eq. (4). The Fabry-Perot resonance wavelengths given by Eq. (6) are shown as solid red lines in Figures 4(a) and 4(b), and show excellent agreement with numerically simulated results for angles of incidence of both 15° and 60° . Because of the nonzero phase shift associated with reflection from the metasurface layer, a Fabry-Perot mode exists even for $m = 0$, in contrast to conventional resonant cavities but consistent with recent studies of enhancement in absorption by a semiconductor deposited on a metal film, for which a nonzero phase is also introduced upon reflection.³⁹

These features are evident in the reflectance and absorption data shown in Figure 4(c), measured at an angle of incidence of 15° for multilayer metasurface structures with SU-8 dielectric layer thickness H ranging from 107 nm to 360 nm. A dip in reflectance, and corresponding peak in absorption, is observed for the $m = 1$ Fabry-Perot resonance at wavelengths in reasonable agreement with those predicted by Eq. (6) for all values of H shown. For larger values of H , similar dips in reflectance and peaks in absorption are observed for the $m = 2$ and for $H = 360$ nm, the $m = 3$ Fabry-Perot resonances as well. For $H = 107$ nm and $H = 121$ nm, elevated absorption at wavelengths of ~ 1000 nm is observed, corresponding to the $m = 0$ Fabry-Perot resonance that arises as a consequence of the nonzero phase shift associated with reflection from each metasurface layer. These Fabry-Perot resonances can be beneficial if increased absorption in the dielectric layer is desired but are detrimental to maximizing reflectivity. In this regard, we note that the reduction in reflectance, and corresponding increase in absorption, is minimized for Fabry-Perot resonances that coincide in wavelength with the Bragg reflection condition. This is most evident in the structure with $H = 185$ nm, for which we see that the reflectance dip and absorption peak associated with the

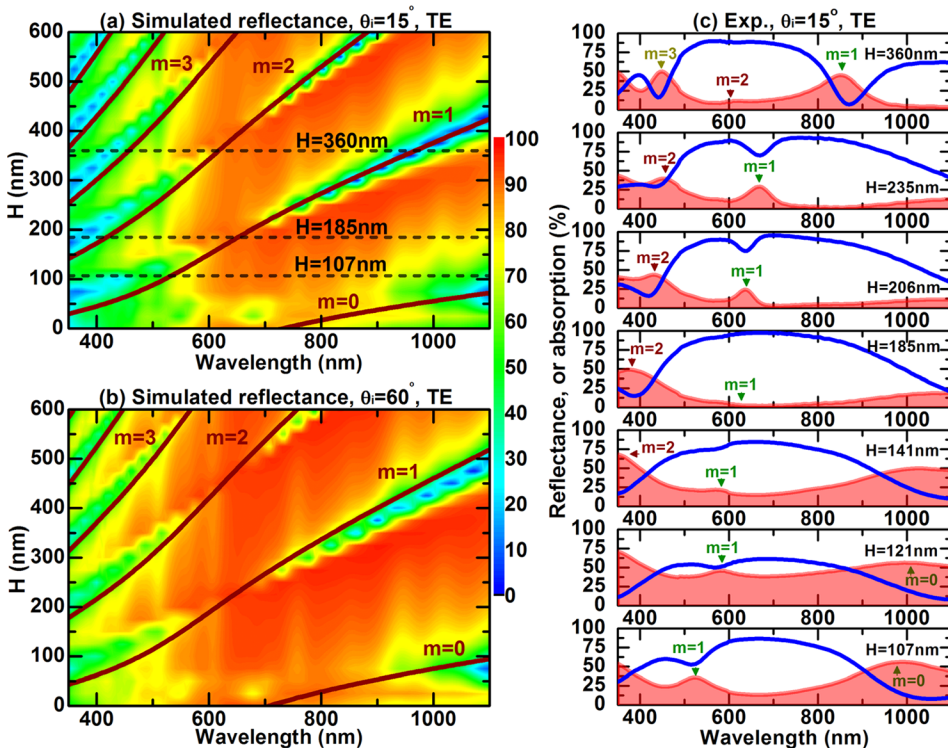


FIG. 4. (a) and (b) Simulated reflectance spectra as a function of wavelength and dielectric layer thickness, H , for $\theta_i = 15^\circ$ and 60° . The solid curves represent the Fabry-Perot resonance given by Eq. (6). The dashed lines are indicated for double layer samples with $H = 360$ nm, 185 nm, 107 nm, respectively. (c) Measured reflectance (solid lines) and absorption (filled lines) for a double layer metasurface with $P = 200$ nm, $D = 160$ nm, $d = 40$ nm, and $h = 10$ nm with different dielectric layer thickness, H , under TE polarized illumination.

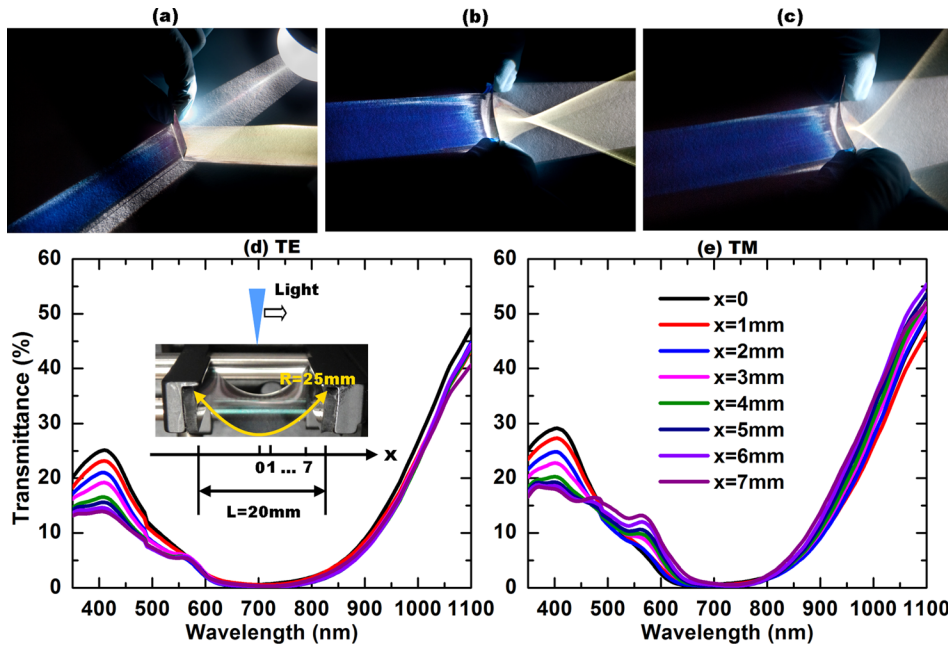


FIG. 5. (a)–(c) Photo taken for samples ($P=200$ nm, $D=160$ nm, $d=40$ nm, $h=10$ nm and $H=185$ nm) held flat, or bent to different curvatures under illumination from a solar simulator to show wavelength-selective focusing by the fabricated multilayer metasurface. (d) and (e) Measured transmittance for a curved double layer metasurface under TE and TM polarized illumination with sample length 25 mm; the end-to-end length is bent to 20 mm. The measurement is taken at different positions of the sample starting from the center to around the edge of the sample, with increment of 1 mm which is roughly the beam size.

$m=1$ Fabry-Perot resonance are strongly suppressed. On this basis, we observe that a broad, high reflectance band is most effectively achieved with a multilayer metasurface structure for which the metasurface plasmonic resonance wavelength λ_r coincides with a Bragg reflection condition. We also emphasize that our multilayer metasurface structure is very robust to variations in vertical alignment in these discussed characteristics since large variations in vertical alignment are expected over the typical beam size (~ 1 mm) in our measurements. This is because the reflection and transmittance properties and Fabry-Perot resonances depend on plasmonic resonance in each individual metasurface layer. Near field coupling between elements in each layer will not play a significant role, when the vertical distance, $H+h$, is large enough, and this is also consistent with previously reported results.^{29,40}

Wavelength-dependent focusing by a flexible, multilayer metasurface structure is shown explicitly in Figure 5. Figure 5(a) shows reflection of a distant, broadband illumination source by a $\sim 2 \times 2.5$ cm² flat multilayer metasurface structure consisting of two metasurface layers with $P=200$ nm, $D=160$ nm, $d=40$ nm, and $h=10$ nm separated by an SU-8 dielectric layer with $H=185$ nm, fabricated on a flexible PET substrate. Short-wavelength blue light (along with infrared light, not visible in the photograph) is transmitted, while light at longer visible wavelengths is reflected. Figures 5(b) and 5(c) show light transmitted and reflected by the same multilayer metasurface structure bent to different curvatures. The reflected light is observed to be focused onto different locations, depending on the degree of curvature of the multilayer metasurface, while the transmitted light remains unfocused and largely unchanged in spectral content. The spectral distribution of the transmitted light at different locations x across a curved multilayer metasurface structure is shown in Figures 5(d) and 5(e), for TE and TM polarization, respectively. As shown in the inset to Figure 5(d), these locations correspond to local angles of

incidence ranging from 0° at $x=0$ mm, corresponding to the midpoint of the curved surface, to $\sim 60^\circ$ at $x=7$ mm, where x is the lateral distance from the midpoint of the curved surface. The transmitted spectra at all locations measured are very similar, differing primarily in that there is a slight decrease in transmittance at short wavelengths as x , and correspondingly the local angle of incidence, is increased. Based on simulations, analytical modeling, and measurements as shown in Figure 4, we attribute this decrease to the development of a Fabry-Perot resonance at shorter wavelengths as the local angle of incidence is increased. The results shown in Figure 5 provide direct confirmation of the ability to perform wavelength-selective imaging and focusing via flexible multilayer metasurface structures, uniformity of optical properties over large (~ 5 cm²) areas, and independence of optical properties to vertical alignment between individual features in adjacent metasurface layers for separations $H+h$ in the range studied here (~ 120 nm and larger).

IV. CONCLUSION

In summary, we have designed, experimentally demonstrated, and analyzed both numerically and analytically a series of flexible, large area, multilayer plasmonic metasurface structures fabricated via nanosphere lithography which provide low loss, wavelength-selective, polarization-independent optical transmittance, reflectance, and focusing of incident light. These characteristics are shown to be robust to vertical misalignment between layers and variations within an individual metasurface layer. The high broad reflectance and low absorption can be understood as the consequence of the constructive Bragg reflection by the multilayer metasurface. Phase shifts associated with each individual metasurface are also examined both experimentally and numerically to show the influence of Fabry-Perot resonance. Finally, wavelength-selective focusing of visible light is also demonstrated.

ACKNOWLEDGMENTS

Part of this work was supported the National Science Foundation (ECCS-1128682 and ECCS-1120823) and the Judson S. Swearingen Regents Chair in Engineering at the University of Texas at Austin. P.-C. Li would like to thank Professor A. Alù (UT-Austin), for discussions on theoretical modeling, H.-H. Kung (Rutgers University) for detailed discussions on NSL, E.-S. Liu (UT-Austin), O. Aved (Molecular Imprint), and S. Singhal (Molecular Imprint) for fruitful discussions and inspirations on fabrication process, K.-F. Lai (UT-Austin) for discussions on experimental setup.

- ¹P.-Y. Chen and A. Alù, *Phys. Rev. B* **84**, 205110 (2011).
- ²F. Monticone, N. M. Estakhri, and A. Alù, *Phys. Rev. Lett.* **110**, 203903 (2013).
- ³N. Yu, P. Genevet, M. A. Kats, F. Aieta, J.-P. Tetienne, F. Capasso, and Z. Gaburro, *Science* **334**, 333 (2011).
- ⁴N. Yu, P. Genevet, F. Aieta, M. A. Kats, R. Blanchard, G. Aoust, J. P. Tetienne, Z. Gaburro, and F. Capasso, *IEEE J. Sel. Top. Quantum Electron.* **19**, 4700423 (2013).
- ⁵W. Cai, U. K. Chettiar, H.-K. Yuan, V. C. de Silva, A. V. Kildishev, V. P. Drachev, and V. M. Shalaev, *Opt. Express* **15**, 3333 (2007).
- ⁶J. B. Lassiter, H. Sobhani, M. W. Knight, W. S. Mielczarek, P. Nordlander, and N. J. Halas, *Nano Lett.* **12**, 1058 (2012).
- ⁷J. Ye, F. Wen, H. Sobhani, J. B. Lassiter, P. V. Dorpe, P. Nordlander, and N. J. Halas, *Nano Lett.* **12**, 1660 (2012).
- ⁸S. H. Mousavi, I. Kholmanov, K. B. Alici, D. Purtseladze, N. Arju, K. Tatar, D. Y. Fozdar, J. W. Suk, Y. Hao, A. B. Khanikaev, R. S. Ruoff, and G. Shvets, *Nano Lett.* **13**, 1111 (2013).
- ⁹C. Wu, A. B. Khanikaev, R. Adato, N. Arju, A. A. Yanik, H. Altug, and G. Shvets, *Nature Mater.* **11**, 69 (2012).
- ¹⁰Y. Zhu, X. Hu, Y. Huang, H. Yang, and Q. Gong, *Adv. Opt. Mater.* **1**, 61 (2013).
- ¹¹Y. Sun, B. Edwards, A. Alù, and N. Engheta, *Nature Mater.* **11**, 208 (2012).
- ¹²Y. Zhao, M. A. Belkin, and A. Alù, *Nat. Commun.* **3**, 870 (2012).
- ¹³J. Valentine, S. Zhang, T. Zentgraf, E. Ulin-Avila, D. A. Genov, G. Bartal, and X. Zhang, *Nature* **455**, 376 (2008).
- ¹⁴N. Liu, M. Hentschel, T. Weiss, A. P. Alivisatos, and H. Giessen, *Science* **332**, 1407 (2011).
- ¹⁵D. Chanda, K. Shigeta, S. Gupta, T. Cain, A. Carlson, A. Mihi, A. J. Baca, G. R. Bogart, P. Braun, and J. A. Rogers, *Nat. Nanotechnol.* **6**, 402 (2011).
- ¹⁶J. Henzie, M. H. Lee, and T. W. Odom, *Nat. Nanotechnol.* **2**, 549 (2007).
- ¹⁷M. H. Lee, M. D. Huntington, W. Zhou, J.-C. Yang, and T. W. Odom, *Nano Lett.* **11**, 311 (2011).
- ¹⁸Z. H. Jiang, S. Yun, F. Toor, D. H. Werner, and T. S. Mayer, *ACS Nano* **5**, 4641 (2011).
- ¹⁹J. B. Pendry, A. Aubry, D. R. Smith, and S. A. Maier, *Science* **337**, 549 (2012).
- ²⁰A. Alù and N. Engheta, *Phys. Rev. E* **72**, 016623 (2005).
- ²¹P.-Y. Chen, J. Soric, and A. Alù, *Adv. Mater.* **24**, OP281 (2012).
- ²²Y. M. Song, Y. Xie, V. Malyarchuk, J. Xiao, I. Jung, K.-J. Choi, Z. Liu, H. Park, C. Lu, R.-H. Kim, R. Li, K. B. Crozier, Y. Huang, and J. A. Rogers, *Nature* **497**, 95 (2013).
- ²³J. Rybczynski, U. Ebels, and M. Giersig, *Colloids Surf. A* **219**, 1 (2003).
- ²⁴C.-C. Ho, P.-Y. Chen, K.-H. Lin, W.-T. Juan, and W.-L. Lee, *ACS Appl. Mater. Interfaces* **3**, 204 (2011).
- ²⁵L. Li, *J. Opt. Soc. Am. A* **14**, 2758 (1997).
- ²⁶A. D. Rakic, A. B. Djuric, J. M. Elazar, and M. L. Majewski, *Appl. Opt.* **37**, 5271 (1998).
- ²⁷E. D. Palik, *Handbook of Optical Constants of Solids* (Academic Press, New York, 1991).
- ²⁸P.-C. Li, Y. Zhao, A. Alu, and E. T. Yu, *Appl. Phys. Lett.* **99**, 221106 (2011).
- ²⁹P.-C. Li and E. T. Yu, *J. Opt. Soc. Am. B* **30**, 27 (2013).
- ³⁰A. Alù, *Optical Wave Interaction With Two-Dimensional Arrays of Plasmonic Nanoparticles* (Cambridge University Press, New York, 2011).
- ³¹E. F. Kuester, M. A. Mohamed, M. Piket-May, and C. L. Holloway, *IEEE Trans. Antennas Propag.* **51**, 2641 (2003).
- ³²J. A. Gordon, C. L. Holloway, and A. Dienstfrey, *IEEE Antennas Wireless Propag. Lett.* **8**, 1127 (2009).
- ³³See supplementary material at <http://dx.doi.org/10.1063/1.4824371> for detailed analytical modeling and discussions.
- ³⁴H. Haug and S. W. Koch, *Quantum Theory of the Optical and Electronic Properties of Semiconductors* (World Scientific, Hong Kong, 1990).
- ³⁵R. Taubert, D. Dregely, T. Stroucken, A. Christ, and H. Giessen, *Nat. Commun.* **3**, 691 (2012).
- ³⁶H. Angus Macleod, *Thin-Film Optical Filter*, 4th ed. (CRC Press, New York, 2010).
- ³⁷M. Born and E. Wolf, *Principles of Optics*, 1st ed. (Pergamon Press, New York, 1959).
- ³⁸R. Taubert, R. Ameling, T. Weiss, A. Christ, and H. Giessen, *Nano Lett.* **11**, 4421 (2011).
- ³⁹M. A. Kats, R. Blanchard, P. Genevet, and F. Capasso, *Nature Mater.* **12**, 20 (2013).
- ⁴⁰A. Christ, O. J. F. Martin, Y. Ekinici, N. A. Gippius, and S. G. Tikhodeev, *Nano Lett.* **8**(8), 2171 (2008).